HHS Public Access

Author manuscript

Structure. Author manuscript; available in PMC 2019 January 02.

Published in final edited form as:

Structure. 2018 January 02; 26(1): 106–117.e6. doi:10.1016/j.str.2017.11.019.

Structural Dynamics Control Allosteric Activation of Cytohesin Family Arf GTPase Exchange Factors

Andrew W. Malaby[1,2,4,5], **Sanchaita Das**[1,5], **Srinivas Chakravarthy**[3], **Thomas C. Irving**[3], **Osman Bilsel**[2], and **David G. Lambright**[1,2,6,*]

[1]Program in Molecular Medicine, University of Massachusetts Medical School, Worcester, MA 01605, USA

[2]Department of Biochemistry and Molecular Pharmacology, University of Massachusetts Medical School, Worcester, MA 01655, USA

[3]The Biophysics Collaborative Access Team (BioCAT), Department of Biological Sciences, Illinois Institute of Technology, Chicago, IL 60616, USA

Summary

Membrane dynamic processes including vesicle biogenesis depend on Arf GTPase activation by guanine nucleotide exchange factors (GEFs) containing a catalytic Sec7 domain and a membrane targeting module such as a PH domain. The catalytic output of cytohesin family Arf GEFs is controlled by autoinhibitory interactions that impede accessibility of the exchange site in the Sec7 domain. These restraints can be relieved through activator Arf-GTP binding to an allosteric site comprising the PH domain and proximal autoinhibitory elements (Sec7-PH linker and C-terminal helix). Small angle X-ray scattering and negative-stain electron microscopy were used to investigate the structural organization and conformational dynamics of Cytohesin-3 (Grp1) in autoinhibited and active states. The results support a model in which hinge dynamics in the autoinhibited state expose the activator site for Arf-GTP binding, while subsequent C-terminal helix unlatching and repositioning unleash conformational entropy in the Sec7-PH linker to drive exposure of the exchange site.

eTOC Blurb

*Correspondence: David.Lambright@umassmed.edu.
[4]Present address: Department of Microbiology and Molecular Genetics, University of Vermont, Burlington, VT 05405, USA
[5]These authors contributed equally
[6]Lead Contact

Author Contributions

Conceptualization, A.W.M, S.D., O.B., and D.G.L.; Methodology, A.W.M, S.D., S.C., T.C.I., O.B., and D.G.L.; Investigation, A.W.M, S.D., and S.C.; Software, A.W.M, S.D., and D.G.L.; Validation, A.W.M, S.D., S.C., and D.G.L.; Formal Analysis, A.W.M, S.D., S.C., and D.G.L.; Resources, S.C. and T.C.I.; Writing – Original Draft, A.W.M, S.D., and D.G.L.; Writing – Review & Editing, A.W.M, S.D., S.C., T.C.I., O.B., and D.G.L.; Visualization, A.W.M, S.D. and D.G.L.; Supervision, T.C.I., O.B., and D.G.L.; Funding Acquisition, T.C.I. and D.G.L.

Arf GTPases control membrane dynamic processes following activation by guanine nucleotide exchange factors (GEFs). Malaby et al. investigate the role of structural dynamics in allosteric activation of Cytohesin family Arf GEFs. Hinge dynamics expose the allosteric site for activator binding whereas conformational entropy drives accessibility of the substrate site.

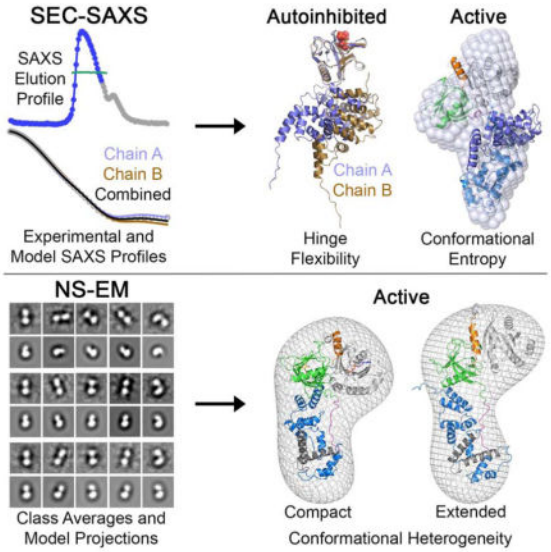

Introduction

Guanine nucleotide exchange factors (GEFs) facilitate conversion of GTPases from inactive GDP-bound to active GTP-bound states (Cherfils and Zeghouf, 2013; DiNitto and Lambright, 2006; Lemmon, 2004). GEFs are commonly regulated through elaborate mechanisms involving post-translational modifications and intra/intermolecular interactions, which can be linked with membrane recruitment for spatiotemporal control of GTPase activation (Aghazadeh et al., 2000; Aizel et al., 2013; Alix et al., 2012; Amor et al., 2005; DiNitto et al., 2007; Gureasko et al., 2008; Gureasko et al., 2010; Malaby et al., 2013; Richardson and Fromme, 2012; Sondermann et al., 2004; Yu et al., 2010).

Arf GTPases have essential roles in numerous cellular processes including vesicle biogenesis, cell migration and metastasis (Donaldson and Honda, 2005; Donaldson and Jackson, 2011; Hashimoto et al., 2004; Muralidharan-Chari et al., 2009; Nie et al., 2003). Membrane association is mediated by insertion of a myristoylated N-terminal amphipathic helix, which docks in a hydrophobic groove in the GDP-bound conformation in solution (Franco et al., 1995; Goldberg, 1998; Liu et al., 2009, 2010; Pasqualato et al., 2001; Randazzo et al., 1995). Nucleotide exchange is catalyzed by the Sec7 domain of Arf GEFs (Casanova, 2007; Chardin et al., 1996). In contrast to truncated Arfs lacking the N-terminal helix, myristoylated Arfs are poor substrates in the absence of membranes. Thus, membrane association of myristoylated Arfs precedes or coincides with catalysis of nucleotide exchange (Franco et al., 1995; Liu et al., 2009, 2010; Randazzo et al., 1995; Renault et al., 2002).

Cytohesins, including the mammalian paralogs cytohesin-1, ARNO and Grp1, are a metazoan Arf GEF family that functions in endocytic trafficking, insulin signaling and other processes at the plasma membrane and endosomes (Fuss et al., 2006; Hafner et al., 2006; Kolanus et al., 1996; Li et al., 2012; Ogasawara et al., 2000). The family is distinguished by a modular architecture with N-terminal heptad repeats (hr), a Sec7 domain, a Pleckstrin Homology (PH) domain, and a C-terminal helix that overlaps with a polybasic region. The exchange activity of the Sec7 domain is potently autoinhibited by the Sec7-PH linker and C-terminal helix, which occlude the catalytic site (DiNitto et al., 2007). Autoinhibition can be relieved by Arf-GTP binding to an allosteric site spanning the PH domain and flanking autoinhibitory elements (Cohen et al., 2007; DiNitto et al., 2007). Arf-GTP binding affinity is enhanced by interaction of the PH domain with phosphatidyl inositol (PtdIns) 3,4,5-tris-phosphate (PIP_3), PtdIns 4,5-bis-phosphate (PIP_2), or their respective head groups IP_4 and IP_3 (Cohen et al., 2007; Dierks et al., 2001; DiNitto et al., 2007). Relief of autoinhibition in solution requires micromolar concentrations of truncated Arf-GTP compared with nanomolar concentrations of myristoylated Arf-GTP on membranes (Cohen et al., 2007; Malaby et al., 2013; Stalder et al., 2011). A distinct autoinhibitory interaction between the heptad repeats and phosphoinositide binding site in the PH domain further regulates membrane recruitment (Hiester and Santy, 2013).

Atomic resolution structures alone and in complexes with Arf GTPases and/or phosphoinositide head groups have been determined for the isolated domains of cytohesins as well as multidomain fragments lacking the heptad repeats or both the heptad repeats and Sec7 domain (Betz et al., 1998; Cherfils et al., 1998; Cronin et al., 2004; DiNitto et al., 2007; Ferguson et al., 2000; Lietzke et al., 2000; Malaby et al., 2013; Renault et al., 2003). In the crystal structure of truncated Arf6-GTP in complex with the Grp1 allosteric site, the linker and C-terminal helix are sequestered in grooves at the core Arf6-GTP/PH domain interface (Malaby et al., 2013). Interpretation of the linker conformation in this structure is complicated by extensive lattice contacts. Hypothetical models for the active complex with Arf6-GTP thus range from ordered conformations predicted to position the Sec7 domain for activation of membrane-associated Arf substrates to dynamic conformations with the domains connected by an intrinsically disordered linker. Since the active constructs are refractory to crystallization, little is known regarding their structural organization and dynamic flexibility. In addition, the crystal structure of autoinhibited Grp1 contains two molecules in the asymmetric unit that differ mainly in the relative orientation of the Sec7 and PH domains. However, the extent of conformational flexibility in the autoinhibited state in solution and potential functional implications have not been investigated.

To gain insight into the structural and dynamic organization of cytohesins, Grp1 constructs and Grp1-Arf6 fusion proteins recapitulating biochemical properties of autoinhibited and active states were analyzed by size exclusion chromatography in-line with small angle X-ray scattering (SEC-SAXS) and by single particle negative stain electron microscopy (NS-EM). Comparison with the crystal structure of autoinhibited Grp1 provides evidence that hinge dynamics expose the activator Arf-GTP site in the autoinhibited state. Rigid body and ensemble analyses further indicate that increased conformational entropy in the Sec7-PH linker coupled to unlatching and repositioning of the C-terminal helix drives exposure of the exchange site for interaction with substrate Arf-GDP without major changes in overall

shape. These observations inform a model for the structural organization and conformational dynamics of cytohesins during membrane recruitment and activation.

Results

Structural organization of autoinhibited and active Grp1 monomers in solution

As an initial step to understand the structural organization of cytohesins in solution and the contribution of conformational dynamics to relief of autoinhibition, SEC-SAXS data sets were acquired for autoinhibited $Grp1_{63-399}$ and fully active $Grp1_{63-390}$ lacking the polybasic region (DiNitto et al., 2007). A minor dimer species previously described for $Grp1_{63-399}$ (Malaby et al., 2015) was also observed for $Grp1_{63-390}$ under similar conditions (Fig. S1). The dimer fraction for $Grp1_{63-399}$ was reduced to an undetectable level by inclusion of 5% glycerol and initiation of SEC-SAXS experiments immediately after concentration. These optimized conditions enhanced signal-to-noise and were subsequently used for other constructs. Regions of the SEC-SAXS data sets that contain only two significant components representing linear combinations of buffer and protein scattering were identified by singular value decomposition (SVD), and the protein scattering reconstructed by Guinier-optimized linear combination (Fig. S1–S3) as described (Malaby et al., 2015).

The crystal structure of autoinhibited $Grp1_{63-399}$ contains two independently refined molecules in the asymmetric unit that differ in the relative orientation of the PH and Sec7 domains (Fig. 1A), despite preserving intramolecular interactions with the linker and C-terminal helix involved in autoinhibition (DiNitto et al., 2007). To determine which if either conformation is compatible with the structure in solution, the experimental SAXS profile was fit with the theoretical profiles calculated from the atomic coordinates using two different algorithms, CRYSOL (Svergun et al., 1995) and FoXS (Schneidman-Duhovny et al., 2013). To eliminate potential discrepancies related to incomplete models, a small number of missing terminal residues, which are disordered in the crystal structure but nevertheless contribute to the solution scattering, were modeled in identical random coil conformations for both molecules. The experimental profile is approximated reasonably well by the calculated profiles for either molecule alone, with no clear distinction (i.e. which molecule fits best depends on the algorithm). Combining the theoretical profiles results in significantly improved agreement with the experimental profile, with the scattering from both molecules contributing almost equally (Fig. 1B). These observations suggest that autoinhibited Grp1 likely adopts more than one conformation in solution related to flexibility in ‘hinge’ residues (^{265}PD^{266} and ^{381}RD^{382}) located at the termini of the PH domain. The functional implications of this conformational variability are discussed below.

Considering the major distinction in autoregulatory status for $Grp1_{63-390}$ and $Grp1_{63-399}$ (DiNitto et al., 2007), differences in standard indicators of size and shape, in particular the radius of gyration (R_G) and pairwise distance distribution (P(r)), are remarkably subtle (Fig. 2A and 2B). *Ab initio* bead models determined by two different algorithms, DAMMIF (Franke and Svergun, 2009) and GASBOR (Svergun et al., 2001), are also similar (Fig. 2C). The bead models for $Grp1_{63-399}$ closely resemble the shape of the corresponding crystal structure, while the bead models for $Grp1_{63-390}$ approximate the shape of the rigid body model calculated with a flexible Sec7-PH linker by CORAL (Petoukhov and Svergun,

2005). Whereas the $Grp1_{63-399}$ SAXS profile is well fit by the combined theoretical profile for the crystal structure (Fig. 1B), substantial systematic deviations are evident in the fit of the $Grp1_{63-390}$ SAXS profile with the combined theoretical profile for the $Grp1_{63-399}$ structure omitting the last nine residues (Fig. 2D), indicative of structural differences beyond truncation of the polybasic region. As an alternative approach, the Ensemble Optimization Method, EOM (Bernado et al., 2007), was used to select ensembles with combined scattering approximating the experimental profile from a deep pool of 100,000 rigid body models with diverse linker conformations. For $Grp1_{63-390}$, the R_G histogram of the selected ensembles is characterized by a broader range and enrichment of more elongated models compared to the pool (Fig. 2E). The best-fitting EOM ensemble has a significantly improved χ^2 compared to the CORAL model (1.08 vs. 1.24), consistent with contributions from three distinct conformations (Fig. 2F). In the CORAL model as well as the two most frequently represented models of the best-fitting EOM ensemble, the catalytic site in the Sec7 domain is accessible to substrates.

Design and Validation of Grp1-Arf6 Fusion Constructs

The crystal structure of the Grp1 allosteric site complex with Arf6-GTP suggested a putative mechanism for relief of autoinhibition involving sequestration of the linker and C-terminal helix at the Arf6/PH domain interface (Malaby et al., 2013). A major unresolved issue concerns how the ordered linker conformation in the crystal structure is influenced by the absence of the Sec7 domain as well as an extensive lattice contact (Fig. 3A). SAXS could provide crucial information regarding the structural organization of Arf6-activated complexes in solution; however, the moderate binding affinity (K_D 15 μM) and rapid off-rate (> 1 s^{-1}) are problematic. An approach for circumventing this impediment was suggested by the ‘Goldilocks’ proximity of the Grp1 C-terminus to the truncated Arf6 N-terminus in the allosteric site complex, a distance readily spanned by the N-terminal helix of Arf6 in a structural model for a Grp1-Arf6 fusion (Fig. 3B). This prediction was explored by generating Grp1-Arf6 fusion constructs with or without a flexible six Gly-Ser linker (Fig. 3C). To support domain assignments in *ab initio* envelopes, equivalent constructs were generated with C-terminal His_6 or SUMO tags. All constructs included an N-terminal His_6 tag for purification as well as the Arf6 Q67L mutation that impairs GTP hydrolysis.

The fusion constructs were loaded with the non-hydrolyzable GTP analog GppNHp and the catalytic efficiency (k_{cat}/K_M) assessed in comparison with isolated $Grp1_{63-399}$ at a near saturating concentration of isolated NΔ13Arf6-GppNHp with and without IP_4, which is required for high affinity binding to the allosteric site (Malaby et al., 2013). With IP_4, the catalytic efficiency of the fusion constructs is comparable to or slightly higher than the isolated proteins (Fig. 3C). Without IP_4, the catalytic efficiency is moderately higher than the isolated proteins, likely due to the high effective concentration of Arf6 in the fusion construct. Catalytic efficiency is substantially reduced by the K340A mutation in the Arf-GTP binding epitope of the PH domain, which was previously shown to impair Arf6-GTP binding and activation (Cohen et al., 2007; Malaby et al., 2013; Stalder et al., 2011). Thus, with IP_4, the fusion constructs have kinetic properties indicative of full activation requiring Arf6-GTP binding to the allosteric site.

SEC-SAXS experiments were conducted with fusion constructs containing the catalytically dead E161A mutation in Sec7 domain (Fig. S2 and S3). The R_G values and P(r) distributions exhibited variations consistent with the size of the C-terminal tag (Fig. 3D and 3E), and were larger/broader than those for $Grp1_{63-399}$. The *ab initio* envelopes calculated with DAMMIF (Fig. 3F) have three prominent features: an elongated volume approximating the Sec7 domain and two similar globular volumes. One of the globular volumes is extended by the addition of SUMO, allowing it to be assigned to Arf6 and the remaining volume to the PH domain.

Ensemble and rigid body analyses of Sec7-PH linker flexibility

To investigate conformational flexibility in the Sec7-PH linker, the scattering profile of the Grp1-Arf6 fusion was analyzed using ensemble (EOM) and rigid body (CORAL) modeling while systematically varying the range of linker residues treated as flexible. The termini of the linker (residues 252-264) are clearly defined by conformational differences in crystal structures of various cytohesin constructs. R_G distributions for the initial pool and selected ensembles are compared in Fig. 4A for representative cases. With only three flexible residues (the number required to connect the Sec7 domain with the ordered linker in the allosteric site complex), the R_G distribution for the selected ensembles is sharply peaked near the maximum of the R_G range for the pool, which contains few models with R_G values close to the experimental value. This observation is consistent with large systematic deviations in the residuals for the best fitting ensemble (Fig. 4B) and even larger deviations for the rigid body model (Fig. 4C). As the number of flexible residues increases, the R_G distributions shift and broaden into a range that includes the experimental R_G, and the systematic deviations in the residuals for the best fitting ensemble and rigid body model are substantially reduced. This behavior is captured at the individual residue level in the χ^2 values for the best fitting ensemble (Fig. 4D), which decrease rapidly as the number of flexible residues increases to approximately eight (first non-flexible residue 260) and diminish more gradually thereafter. Similar trends are observed for the fusion construct with a six Gly-Ser linker and for the best fitting minimal ensembles selected by an alternative algorithm, MultiFoXS (Carter et al., 2015), from an independently generated pool. Conversely, no systematic variation was observed for an equivalent control analysis of flexibility in the linker for autoinhibited $Grp1_{63-399}$. The best fitting EOM ensemble for 260 as the first non-flexible linker residue consists of two models, with the most frequent model resembling the *ab initio* envelope (Fig. 4E). In both EOM models, and also in the rigid body CORAL model as well as the most frequent model of the best fitting MultiFoXS ensemble, the exchange site in the Sec7 domain is unobstructed.

Single particle negative-stain electron microscopy of an active Grp1-Arf6 fusion construct

As an independent approach, the structural organization and conformational variability of the Grp1-Arf6 fusion bound to IP_4 was investigated by NS-EM. The peak fraction after size exclusion chromatography on Superdex-200 was immediately diluted, applied to carbon coated grids, and stained with uranyl formate to enhance contrast (Fig. S4). Individual particles with a variety of orientations and/or shapes were observed on raw micrographs (Fig. 5A and 5B). Unsupervised classification of ~10,000 manually picked particles from 369 micrographs yielded 71 good quality classes representing ~6500 particles (Fig. 5C).

Analysis of conformational heterogeneity in 2D particle classes

The different class averages reflect a variety of projected shapes hypothesized to represent alternate views of an asymmetrical multidomain protein, which may sample one or more conformations. In the case of multiple conformations, each particle class would be expected to comprise similar views of particles in similar conformations. To simultaneously test whether the class averages are consistent with views of an active Grp1-Arf6 fusion and provide an initial assessment of the extent of conformational diversity, the class averages were systematically compared with 3D volume projections generated in 10° angular increments over the range of possible views for the MultiFoXS pools with 255, 260 or 265 as the first non-flexible residue in the Sec7-PH linker (Fig. 6A and S5). As with the corresponding MultiFoXS analyses of the SAXS profile, the best scoring models span R_G ranges similar to those of the pools, with a preference for larger values (Fig. 6B). Notably, the quality of the comparisons improves substantially as the number of flexible residues increases (Fig. 6C and 6D). For 265 as the first non-flexible residue, the best scoring model/projection for each class strongly resembles the class average, indicating that the conformational diversity within the pool is sufficient to represent the range of 2D classes.

3D reconstructions and analysis of conformational heterogeneity

Initial attempts to generate a single 3D reconstruction with visually selected particle classes potentially corresponding to different views were unsuccessful, likely due to excessive conformational heterogeneity. Consistent with that explanation, 3D volumes could be built and refined for two sets of classes selected as relatively compact or relatively extended based on inspection of the best scoring models from the comparison with the class averages (Fig. 7A and S6). The low resolution of approximately 35–40 Å for the refined 3D reconstructions (Fig. S7) may be due in part to negative staining but is also likely to be limited by conformational heterogeneity, as reflected in the broad range of R_G values for the best scoring models obtained from comparison of the MultiFoXS pool with the 2D class averages. Automated unbiased rigid body docking of the MultiFoXS pools with 255, 260 and 265 as the first non-flexible linker residue was conducted for the refined 3D volumes reconstructed using the relatively compact and extended class sets (Fig. 7A and S6). For both volumes, the quality of the fits improved as the number of flexible linker residues increased (Fig. 7B). As with the corresponding SAXS analysis, the largest improvement was observed when the first non-flexible linker residue was shifted from 255 to 260. For the compact volume, the best fits with the 260 pool are slightly better than those for the 265 pool. The simplest explanation for these observations is that the represented classes for the compact volume correspond to conformations with the C-terminal linker residues docked at the Arf6-PH domain interface as in the crystal structure of the allosteric site complex whereas the represented classes for the extended volume corresponded to more flexible undocked conformations.

Discussion

The structural dynamic organization of Grp1 conformations in active and autoinhibited states was investigated by SEC-SAXS and NS-EM. Rigid body and ensemble analyses based on atomic resolution structures were crucial for insights beyond overall size and shape.

Comparison of active Grp1 constructs lacking the polybasic region with the corresponding autoinhibited constructs indicates that large conformational rearrangements coupled to increased linker flexibility are sufficient to expose the exchange site in the Sec7 domain, without major differences in shape.

Systematic rigid body and ensemble analyses of monomeric Grp1-Arf6 fusions retaining distinctive hallmarks of the isolated protein complex provide compelling evidence that the Sec7-PH linker is considerably more flexible in solution than suggested by the crystal structure of the allosteric site complex, a discrepancy attributable to the absence of the Sec7 domain and lattice contacts with the linker. The requirement for flexibility is most acutely related to linker residues 252-260, which contribute to autoinhibition but are dispensable for Arf6-GTP binding affinity (DiNitto et al., 2007; Malaby et al., 2013). Conversely, increasing flexibility beyond residue 260 has a marginal effect on the quality of the rigid body and ensemble fits, consistent with the packing of ^{261}Thr-Phe^{262} at the PH-Arf6 interface and five-fold reduction in Arf6-GTP binding affinity accompanying truncation of residues 260-264 (Malaby et al., 2013). A similar overall trend was observed for comparisons with NS-EM class averages and reconstructed volumes, which improved with increased linker flexibility. The volume comparisons further suggest the presence of two conformational populations, one with the C-terminal linker residues docked at the Arf6-PH domain interface and another with a fully flexible linker.

The preceding observations inform a structural dynamic model for the major conformational intermediates of the cytohesin autoregulatory core during membrane recruitment and allosteric activation (Fig. 8). After initial membrane recruitment, involving specific phosphoinositide-binding augmented by non-specific interactions with the phospholipid bilayer, the autoinhibited core samples a range of catalytically incompetent conformations related to dynamic flexibility of PH domain-proximal ‘hinge’ residues that do not participate in autoinhibitory interactions. In some of these hinge conformations, represented by chain A in the autoinhibited Grp1 crystal structure, activator Arf-GTP binding is impeded by steric collision with the C-terminal helix. In other hinge conformations, represented by chain B, the activator binding site in the PH domain is accessible. Lateral association of membrane-bound activator Arf-GTP with the PH domain in accessible hinge conformations may facilitate formation of an intermediate complex with the activator Arf-GTP. Intramolecular rearrangements involving release of the C-terminal helix from the catalytic site and subsequent docking at the PH domain interface with the activator Arf-GTP stabilize the membrane-targeted complex in an ‘unlatched’ state where the linker is free to sample a broad range of configurations. Many of the unlatched conformations expose the substrate site and in some cases, represented by the most frequent MultiFoXS model for the pool with 260 as the first non-flexible linker residue, the Sec7 domain would be appropriately oriented for lateral association with membrane-bound substrate Arf-GDP. In addition to enhancing the stability of the complex, docking of the C-terminal linker residues at the PH domain interface with the activator Arf-GTP would favor membrane proximal orientations of the Sec7 domain by restricting the configurational space sampled by the linker.

Alternative pathways for allosteric activation are possible in principle. For example, unlatching of the C-terminal helix might precede activator Arf-GTP binding. The proposed

'activator binding first' pathway may be more efficient, since the SAXS analysis suggests that the activator site in the PH domain is accessible in approximately half of the autoinhibited Grp1 population whereas only a small fraction of unlatched Grp1 (estimated as ~0.01 from the catalytic efficiencies of autoinhibited and fully active constructs (DiNitto et al., 2007)) is available for activator Arf6-binding. In either case, activator Arf-GTP binding to the PH domain presumably occurs before docking of the C-terminal helix at the PH domain-Arf6 interface.

The SAXS and NS-EM experiments presented here provide mechanistic insights into the structural dynamic organization of the autoregulatory core of cytohesins in active vs. inactive states. Additional studies will be required to understand the quaternary organization of cytohesins in homo- as well as heterodimeric complexes.

STAR Methods

CONTACT FOR REAGENT AND RESOURCE SHARING

Further information and requests for resources and reagents should be directed to and will be fulfilled by the Lead Contact, David Lambright (David.Lambright@umassmed.edu).

EXPERIMENTAL MODEL AND SUBJECT DETAILS

Mouse Grp1 (diglycine splice variant) constructs and fusion constructs with human Arf6 Q67L were expressed in the bacterial strain BL21(DE3). The amino acid sequences for human and mouse Arf6 are identical.

METHOD DETAILS

Constructs, Expression and Purification—Constructs were amplified using Vent polymerase, digested with BamHI and SalI or XhoI, and ligated into modified pET15b vectors. Mutations were generated using whole plasmid PCR supplemented with QuikSolution (Stratagene) followed by DpnI digestion (NEB). BL21(DE3) cells (Novagen) were transformed with plasmids, grown in 2xYT with 100 mg/L ampicillin to OD_{600} 0.2–0.4, and induced with 50 μM IPTG for 14–18 hrs at 18°C. Cells pellets were resuspended in buffer (50 mM Tris pH 8.0, 150 mM NaCl, 2 mM $MgCl_2$, 0.05% 2-mercaptoethanol) and incubated with 0.1 mM PMSF, 0.2 mg/ml lysozyme, and 0.01 mg/ml protease free DNAse I (Worthington). Lysates were sonicated, centrifuged at 30,000×g for 1 hr with 0.5% Triton X-100 and purified over Ni-NTA followed by ion exchange with HiTrap SP or Q, and gel filtration on Superdex-75 or 200 (GE Healthcare).

Nucleotide Loading—Samples were incubated in 20 mM Tris, pH 8.0, 150 mM NaCl, 5 mM EDTA, and 1 mM DTT with a 10 fold molar excess of GppNHp or mantGDP. $MgCl_2$ was added to 10 mM and excess nucleotide removed by gel filtration.

GEF Assays—Grp1 and Grp1-Arf6 fusion constructs with or without 80 μM Arf6NΔ13-GppNHp or 10 μM IP_4 were formatted into 96 well half area microplates (Corning) and incubated for 16–24 hrs at 25°C in 20 mM Tris, pH 8.0, 150 mM NaCl, 2 mM $MgCl_2$ and 250 μM GppNHp. Exchange reactions were initiated by addition of 1 μM Arf1NΔ17-

mantGDP and monitored using a Safire microplate spectrophotometer (Tecan) with excitation at 360 nm and emission at 440 nm. Observed rate constants (k_{obs}) were obtained by fitting with $I_t = (I_0 - I_\infty) \exp(-k_{obs}\, t) + I_\infty$, where I_t, I_0, and I_∞ are the emission intensities at times t, t = 0, and $t \rightarrow \infty$. Catalytic efficiencies (k_{cat}/K_M) were obtained from the slope of a linear least squares fit with $k_{obs} = (k_{cat}/K_M)\,[GEF] + k_{intr}$, where k_{intr} is the intrinsic rate constant.

SEC-SAXS Data Collection and Processing—SEC-SAXS data sets were collected at the BioCAT Sector 18-ID beamline at the Argonne National Laboratory Advanced Photon Source. Samples were incubated with a 1.2 molar excess of IP_4 for 1–5 hrs, concentrated to 10–20 mg/ml and injected onto 24 ml Superdex-200 ($Grp1_{63\text{-}390}$) or 3 ml Superdex-200 Increase columns (GE Healthcare) equilibrated with 20 mM Tris, pH 8.0, 150 mM NaCl, 2 mM $MgCl_2$, 0.1% 2-mercaptoethanol, 5% glycerol, and 1 μM IP_4. Column outlets were connected to the flow cell and SAXS data sets acquired with 1 s exposures at 5 s intervals during elution. Raw SAXS images were radially averaged on a log scale over the q range 0.00825–0.413 ($Grp1_{63\text{-}390}$) or 0.00621–0.333 $Å^{-1}$, normalized by the incident beam intensity, and further processed to reconstruct the 1D scattering profiles for the protein by buffer subtraction with or without automatic determination of an optional scaling constant or by singular value decomposition and linear combination (SVD-LC) as described (Malaby et al., 2015). For SVD-LC, the data matrix **A** with columns corresponding to normalized 1D scattering profiles for selected regions of the SEC-SAXS elution profile were decomposed by SVD as $\mathbf{A} = \mathbf{U} \cdot \mathbf{S} \cdot \mathbf{V}^T$. The columns of the matrix **U** contain orthonormal basis components that span the vector space of **A** and are further rotated to successively maximize the contribution of each component; the elements of the diagonal matrix **S** contain weights (known as singular values) for the components; and the orthonormal columns of the symmetric matrix **V** (before transposition denoted by T) contain the normalized contributions of the component to each column of **A**. The analysis presented in Figures S1–S3 indicates that the selected regions of the SEC-SAXS elution profiles used for SVD-LC contain only two significant components, corresponding to linear combinations of scattering from the buffer/sample cell and protein, with the remaining components representing noise. Protein scattering profiles were reconstructed as <I(q) peak region> - <I(q) buffer region(s)> for direct subtraction, <I(q) peak region> - c * <I(q) buffer region(s)> for optimized subtraction, and $c * U_0 + U_1$ for SVD-LC. Here, the angle brackets <> denote averages of the scattering profiles in the peaks or buffer regions. Optimal values for the scaling constant/coefficient c were automatically determined by systematic analysis of linearity in the Guinier region as a function of the buffer scale factor for optimized buffer subtraction or the U_0 coefficient for linear combination of the two most significant SVD components. In each case, the SVD-LC profiles had superior signal-to-noise, fewer subtraction artifacts, and were used for subsequent analyses.

Theoretical and Ab Initio Modeling—SAXS profiles were fit with theoretical scattering profiles calculated from atomic coordinates using CRYSOL (Svergun et al., 1995) or FoXS (Schneidman-Duhovny et al., 2013). Combined fits were calculated as a maximum likelihood linear combination of the individual fits in DELA (Malaby et al., 2015). P(r) distributions were calculated using GNOM (Svergun, 1992) in PRIMUS (Konarev et al.,

2003). *Ab initio* bead models were calculated using DAMMIF (Franke and Svergun, 2009) and GASBOR (Svergun et al., 2001). Typically, 100 bead models were averaged/filtered in groups of 10 using DAMAVER (Volkov and Svergun, 2003) and the process repeated on the averaged/filtered models to generate the final models, which were aligned with atomic coordinates using SUPCOMB (Kozin and Svergun, 2001).

Rigid Body and Ensemble Modeling—Initial models were derived from crystal structures of $Grp1_{63-399}$ (2R09) and the Grp1-Arf6 allosteric site complex (2KAX). Missing linker and terminal elements were included with MODELLER (Webb and Sali, 2014) in CHIMERA (Pettersen et al., 2004). Rigid body modeling was performed with CORAL (Petoukhov et al., 2012). For ensemble modeling with EOM (Tria et al., 2015), 10,000 models were generated with RANCH and ensembles selected using GAJOE. For ensemble analyses with MultiFoXS, 10,000 models was generated using RRT_SAMPLE (Raveh et al., 2009). To include the head group, the relevant atoms were renamed as atoms in dummy glycine residues that retained the chemical information in the last column of the PDB file required to specify the correct scattering form factors. Scattering profiles were calculated with FoXS (Schneidman-Duhovny et al., 2013) and best fitting single or multi-model ensembles determined using MultiFoXS (Carter et al., 2015) using the IMP (Russel et al., 2012) command line tools RRT_SAMPLE, foxs and multi_foxs.

EM Sample Preparation and Negative Staining—Grp1-Arf6 loaded with GppNHp was incubated with IP_4 for 2 hrs prior to concentration and size exclusion chromatography on a Superdex-200 column (GE Healthcare) equilibrated with 20 mM Tris, pH 8.0, 150 mM NaCl, 2 mM $MgCl_2$, 0.1% 2-mercaptoethanol, and 1 μM IP_4. Protein from the peak fraction was immediately diluted, applied to glow discharged carbon coated Gilder copper 400 mesh grids (EM Sciences), incubated for 1 min, rinsed with deionized water, and stained with 0.75% (w/v) uranyl formate (EM Sciences) as described (Booth et al., 2011). Images were acquired on a Technai F12 electron microscope operated at 120 kV using a Gatan Erlang Shen 785 camera with a nominal magnification of 60,000, corresponding to a calibrated pixel size of 3.5 Å at the specimen level. A total of 369 micrographs were collected with a nominal defocus range of −1.2 to −3.2 μm and a low dose of ~20–30 electrons/Å.

Image Processing—Images were processed with EMAN2 (Tang et al., 2007) after X-ray removal with IMOD (Kremer et al., 1996). Approximately 10,000 particles were manually picked with a box size of 80×80 pixels. Following contrast transfer function (CTF) fitting and preprocessing of extracted images, particle sets were built. One hundred 2D class averages were generated by unsupervised reference-free image refinement. Seventy one classes comprising 6504 particles remained after eliminating bad classes. Initial models were built for 22 compact and 20 extended classes. Final 3D refinement with full CTF correction against the starting models was carried out by the gold-standard procedure in EMAN2. The resolution of the refined 3D reconstructions was estimated as 35–40 Å based on a Fourier shell correlation (FSC) cut-off of 0.5 (Rosenthal and Henderson, 2003) and by comparison of volumes for best fitting structural models calculated in 5 Å resolution increments in Chimera (Figure S7). The refined 3D volumes were validated by EMAN2 validation methods.

2D Class Average and 3D Volume Analyses—Atomic resolution models were converted to 40 Å resolution volumes with EMAN2 e2pdb2mrc and volume projections compared with 2D class averages at 10° increments using EMAN2 e2classsvsproj. Two python scripts (e2pdbs2mrcs and e2classesvsprojs_best_scores) were developed to automate these steps and rank order models based on best scoring projections for each class. For comparison with 3D volumes, automated rigid body docking of models at a resolution of 35 Å was performed with ADP_EM (Garzon et al., 2007). Models and volumes were visualized in Chimera (Pettersen et al., 2004).

Software Resources—Software available through the SBGRID Consortium was used for supported applications (Morin et al., 2013).

QUANTIFICATION AND STATISTICAL ANALYSIS

GEF Assays—Catalytic efficiencies and error bars plotted in Figure 3C are the mean and standard deviation of three independent experiments. See GEF Assays under Method Details for description of the kinetics analysis used to determine catalytic efficiencies.

SAXS Profiles—Errors for SAXS profiles were estimated in DELA using a second order polynomial fit over an 11 point window centered on each point in the SAXS profile. In some cases, errors were re-estimated as the root mean squared deviation of the residuals for the fit with a maximum entropy model for the discretized inverse pair-distribution transformation

$$I(q)=4\pi \sum P(r)\sin(qr)/qr$$

calculated on a real space grid of 1 Å over the range from 0.01 Å to an upper limit approximately 10–20% larger than D_{max}. The informational entropy was calculated using a sine function on the interval 0-π radians as the prior distribution. The χ^2 values reported here thus reflect the quality of fits with theoretical, rigid body and ensemble models compared to the nearly ideal best fit attainable with the maximum entropy inverse pair-distribution model. This approach for estimating errors avoids non-trivial and likely inaccurate error propagation associated with SVD-LC reconstruction of SAXS profiles.

Comparison with Class Averages and Volumes—Correlation coefficients and scoring functions for comparison of 2D class averages and 3D volumes with projections and volumes derived from atomic coordinates are presented as calculated by the software applications described in the Method Details and in the references therein.

DATA AND SOFTWARE AVAILABILITY

Data and Model Depositions—SAXS profiles, P(r) distributions, fits and models have been deposited with the Small Angle Scattering Biological Data Bank (Valentini et al., 2015) under the accession codes SASDCK7 (Grp1 63-399), SASDCL7 (Grp1 63-390), SASDCM7 (Grp1 63-399 E161A 6GS Arf6 Q67L), SASDCN7 (Grp1 63-399 E161A 6GS Arf6 Q67L His6), SASDCP7 (Grp1 63-399 E161A 6GS Arf6 Q67L SUMO), and SASDCQ7 (Grp1 63-399 E161A Arf6 Q67L). EM envelopes have been deposited with the EM Data Bank

(Lawson et al., 2016) under the accession codes EMD-7077 (Grp1 63-399 E161A Arf6 Q67L Compact Volume) and EMD-7078 (Grp1 63-399 E161A Arf6 Q67L Extended Volume). The best-fitting MultiFoXS models selected by ADP_EM have been deposited with the Protein Data Bank (Berman et al., 2000) under the accession codes 6BBP (Grp1 63-399 E161A Arf6 Q67L best-fitting MultiFoXS model for Compact Volume) and 6BBQ (Grp1 63-399 E161A Arf6 Q67L best-fitting MultiFoXS model for Extended Volume). The geometry of the modeled regions was improved using MODELLER during deposition to the PDB; however, these changes did not affect the orientation or correlation score for the fits with ADP_EM. Accession codes for the depositions are also listed in the Key Resources Table. Other data and models are available on request to the Lead Contact.

Software—The Mac OSX application DELA and associated Python scripts for processing and analysis of SAXS and SEC-SAXS profiles have been described previously (Malaby et al., 2015). The Python scripts (.py), bash shell scripts (.sh), and “pipelines” (_pipeline.txt) for SAXS and EM analyses described below can be downloaded as a zip file (Data S1), which also includes the application bundle and associated Python scripts for DELA. Although these scripts and pipelines are distributed as Open Source (https://opensource.org), the command line tools, programs or source code executed by these automation scripts are subject to the licensing terms of the relevant packages.

Shell Scripts

dammif.sh: Automates generation of *ab initio* bead models with DAMMIF, systematic pairwise alignment and selection with DAMSEL, alignment against the most representative bead model with DAMSUP, ‘averaging’ with DAMAVER, filtering with DAMFILT, and generation of an input file for DAMMIN with DAMSTART.

gasbor.sh: Equivalent to dammif.sh except that generation of *ab initio* bead models is done with GASBOR.

foxs.sh: Automates calculation of SAXS profiles using the command line version FoXS. Can be run in parallel batches.

Python Scripts

multifoxs_filenames.py: Generates a file containing the filenames for input to the command line version of multi_foxs.

e2pdbs2mrcs.py: Automates generation of volumes from atomic coordinates using the EMAN2 python script e2pdb2mrc.py. Can be run in parallel batches.

e2classesvsprojs.py: Automates comparison of class averages with volume projections using the EMAN2 python script e2classvsproj.py. Can be run in parallel batches.

e2classesvsprojs_best_scores.py: Identifies the best score and volume projection for each class average as well as the overall best score and volume projection for all class averages using the output of e2classesvsprojs.py.

e2classesvsprojs_extract_best.py: Extracts the best scoring coordinate files and corresponding image stacks using the output of e2classesvsprojs_best_scores.py.

e2classesvsprojs_generate_best_list.py: Generates a list of the images for the best scoring volume projection versus class average comparisons using the output of e2classesvsprojs_best_scores.py. The resulting list in "fast LST format" can be used as input for compilation of the images into an image stack in EMAN2.

Pipelines—The following "pipelines" are intended to illustrate the sequence of command line tools and scripts. Although they can be converted to a fully automated shell script if desired, we prefer to run the instructions individually to allow the output at each step to be monitored for quality control.

multifoxs_pipeline.txt: Example "pipeline" illustrating the sequence of command line instructions used for Multi_FoXS model generation, profile calculation and analysis with the IMP command line tools RRT_SAMPLE, foxs, and multi_foxs.

e2classesvsprojs_pipeline.txt: Example "pipeline" illustrating sequence of command line instructions used for Multi_FoXS model generation, profile calculation and multicomponent analysis.

KEY RESOURCES TABLE

The table highlights the genetically modified organisms and strains, cell lines, reagents, software, and source data **essential** to reproduce results presented in the manuscript. Depending on the nature of the study, this may include standard laboratory materials (i.e., food chow for metabolism studies), but the Table is **not** meant to be comprehensive list of all materials and resources used (e.g., essential chemicals such as SDS, sucrose, or standard culture media don't need to be listed in the Table). **Items in the Table must also be reported in the Method Details section within the context of their use.** The number of **primers and RNA sequences** that may be listed in the Table is restricted to no more than ten each. If there are more than ten primers or RNA sequences to report, please provide this information as a supplementary document and reference this file (e.g., See Table S1 for XX) in the Key Resources Table.

Please note that ALL references cited in the Key Resources Table ***must be included in the References list.*** Please report the information as follows:

- **REAGENT or RESOURCE:** Provide full descriptive name of the item so that it can be identified and linked with its description in the manuscript (e.g., provide version number for software, host source for antibody, strain name). In the Experimental Models section, please include all models used in the paper and describe each line/strain as: model organism: name used for strain/line in paper: genotype. (i.e., Mouse: $OXTR^{fl/fl}$: B6.129(SJL)-$Oxtr^{tm1.1Wsy/J}$). In the Biological Samples section, please list all samples obtained from commercial sources or biological repositories. Please note that software mentioned in the Methods Details or Data and Software Availability section needs to be also included in the

table. See the sample Table at the end of this document for examples of how to report reagents.

- **SOURCE:** Report the company, manufacturer, or individual that provided the item or where the item can obtained (e.g., stock center or repository). For materials distributed by Addgene, please cite the article describing the plasmid and include “Addgene” as part of the identifier. If an item is from another lab, please include the name of the principal investigator and a citation if it has been previously published. If the material is being reported for the first time in the current paper, please indicate as “this paper.” For software, please provide the company name if it is commercially available or cite the paper in which it has been initially described.
- **IDENTIFIER:** Include catalog numbers (entered in the column as “Cat#” followed by the number, e.g., Cat#3879S). Where available, please include unique entities such as RRIDs, Model Organism Database numbers, accession numbers, and PDB or CAS IDs. For antibodies, if applicable and available, please also include the lot number or clone identity. For software or data resources, please include the URL where the resource can be downloaded. Please ensure accuracy of the identifiers, as they are essential for generation of hyperlinks to external sources when available. Please see the Elsevier list of Data Repositories with automated bidirectional linking for details. When listing more than one identifier for the same item, use semicolons to separate them (e.g. Cat#3879S; RRID: AB_2255011). If an identifier is not available, please enter “N/A” in the column.
  - ***A NOTE ABOUT RRIDs:*** We highly recommend using RRIDs as the identifier (in particular for antibodies and organisms, but also for software tools and databases). For more details on how to obtain or generate an RRID for existing or newly generated resources, please visit the RII or search for RRIDs.

Please use the empty table that follows to organize the information in the sections defined by the subheading, skipping sections not relevant to your study. Please do not add subheadings. To add a row, place the cursor at the end of the row above where you would like to add the row, just outside the right border of the table. Then press the ENTER key to add the row. You do not need to delete empty rows. Each entry must be on a separate row; do not list multiple items in a single table cell. Please see the sample table at the end of this document for examples of how reagents should be cited.

KEY RESOURCES TABLE

REAGENT or RESOURCE	SOURCE	IDENTIFIER
Antibodies		
Bacterial and Virus Strains		
BL21(DE3) Competent Cells	Novagen	Cat#69450

REAGENT or RESOURCE	SOURCE	IDENTIFIER
XL-10 Gold Ultracompetent Cells	Agilent	Cat#200314
Biological Samples		
Chemicals, Peptides, and Recombinant Proteins		
Mant-GDP	Jena Biosciences	Cat#NU-204L
GppNHp	Jena Biosciences	Cat#NU-899-10
Inositol 1,3,4,5 tetrakis-phosphate, Potassium Salt (IP4)	Cell Signals	Cat#803
Uranyl Formate	EM Sciences	Cat#22450
Critical Commercial Assays		
Wizard Plus Miniprep DNA Purification Kit	Promega	Cat#A7510
Wizard SV Gel and PCR Cleanup Kit	Promega	Cat#A9281
Deposited Data		
Grp1 63-399 SAXS	This Paper	SASDCK7 https://www.sasbdb.org
Grp1 63-390 SAXS	This Paper	SASDCL7 https://www.sasbdb.org
Grp1 63-399 E161A 6GS Arf6 Q67L SAXS	This Paper	SASDCM7 https://www.sasbdb.org
Grp1 63-399 E161A 6GS Arf6 Q67L His6 SAXS	This Paper	SASDCN7 https://www.sasbdb.org
Grp1 63-399 E161A 6GS Arf6 Q67L SUMO SAXS	This Paper	SASDCP7 https://www.sasbdb.org
Grp1 63-399 E161A Arf6 Q67L SAXS	This Paper	SASDCQ7 https://www.sasbdb.org
Grp1 63-399 E161A Arf6 Q67L Compact Volume	This Paper	EMD-7077 http://www.emdatabank.org
Grp1 63-399 E161A Arf6 Q67L Extended Volume	This Paper	EMD-7078 http://www.emdatabank.org
Grp1 63-399 E161A Arf6 Q67L best-fitting MultiFoXS model for Compact Volume	This Paper	PDB: 6BBP http://www.rcsb.org
Grp1 63-399 E161A Arf6 Q67L best-fitting MultiFoXS model for Extended Volume	This Paper	PDB: 6BBQ http://www.rcsb.org
Experimental Models: Cell Lines		
Experimental Models: Organisms/Strains		
Oligonucleotides		
Recombinant DNA		
Plasmid: Modified pET15 (pDL2)	DiNitto, 2007	N/A
Plasmid: Modified pET15 with C-term SUMO tag (pDL2-SUMO)	This Paper	N/A
Plasmid: Modified pET15 plasmid with C-term His (pDL2-His)	This Paper	N/A

REAGENT or RESOURCE	SOURCE	IDENTIFIER
Mouse Grp1 63-399 in pDL2	DiNitto, 2007	N/A
Mouse Grp1 63-390 in pDL2	DiNitto, 2007	N/A
Mouse Grp1 63-399 human Arf6 Q67L in pDL2, pDL2-SUMO and pDL2-His	This Paper	N/A
Mouse Grp1 63-399 E161A human Arf6 Q67L in pDL2, pDL2-SUMO and pDL2-His	This Paper	N/A
Mouse Grp1 63-399 K340A human Arf6 Q67L in pDL2, pDL2-SUMO and pDL2-His	This Paper	N/A
Mouse Grp1 63-399 6GS human Arf6 Q67L in pDL2, pDL2-SUMO and pDL2-His	This Paper	N/A
Mouse Grp1 63-399 E161A 6GS human Arf6 Q67L in pDL2, pDL2-SUMO and pDL2-His	This Paper	N/A
Mouse Grp1 63-399 K340A 6GS human Arf6 Q67L in pDL2, pDL2-SUMO and pDL2-His	This Paper	N/A
Software and Algorithms		
ADP_EM	Garzón et al, 2007	http://chaconlab.org/hybrid4em/adp-em
ATSAS	Pethoukhov, 2012	www.embl-hamburg.de/biosaxs/software.html
CHIMERA	Pettersen, 2004	https://www.cgl.ucsf.edu/chimera/download.html
CORAL	Petoukhov, 2012	www.embl-hamburg.de/biosaxs/software.html
CRYSOL	Svergun, 1995	www.embl-hamburg.de/biosaxs/software.html
DAMAVER (DAMSEL, DAMSUP, DAMAVER and DAMFILT)	Volkov, 2003	www.embl-hamburg.de/biosaxs/software.html
DAMMIF	Franke, 2009	www.embl-hamburg.de/biosaxs/software.html
DELA	Malaby, 2015	DOI: 10.1107/S1600576715010420
EMAN2	Tang et al., 2007	http://blake.bcm.edu/emanwiki/EMAN2
EOM (RANCH and GAJOE)	Tria, 2015	www.embl-hamburg.de/biosaxs/software.html
FoXS	Schneidman-Duhovny, 2013	https://integrativemodeling.org
GASBOR	Svergun, 2001	www.embl-hamburg.de/biosaxs/software.html
GNOM	Svergun, 1992	www.embl-hamburg.de/biosaxs/software.html
IMOD	Kremer et al., 1996	http://bio3d.colorado.edu/imod/
IMP	Russel, 2012	https://integrativemodeling.org
MODELLER	Webb, 2014	https://salilab.org/modeller/
MultiFoXS	Carter, 2015	https://integrativemodeling.org
PRIMUS	Konarev, 2003	www.embl-hamburg.de/biosaxs/software.html
PyMol	SBGRID	https://pymol.org
RRT_SAMPLE	Raveh, 2009	https://integrativemodeling.org
SBGRID	Morin, 2013	https://sbgrid.org
SUPCOMB	Kozin, 2001	www.embl-hamburg.de/biosaxs/software.html
dammif.sh	This paper	N/A

REAGENT or RESOURCE	SOURCE	IDENTIFIER
e2classvsproj.py	EMAN2	N/A
e2classesvsprojs.py	This paper	N/A
e2classesvsprojs_best_scores.py	This paper	N/A
e2classesvsprojs_extract_best.py	This paper	N/A
e2classesvsprojs_generate_best_list.py	This paper	N/A
e2pdb2mrc.py	EMAN2	N/A
e2pdbs2mrcs.py	This paper	N/A
e2classesvsprojs_pipeline.txt	This paper	N/A
filenames.py	This paper	N/A
gasbor.sh	This paper	N/A
foxs.sh	This paper	N/A
multifoxs_pipeline.txt	This paper	N/A
Other		
HiTrap Q HP	GE Healthcare Life Sciences	Cat#17-1154-01
HiTrap SP HP	GE Healthcare Life Sciences	Cat#17115201
His-Trap HP	GE Healthcare Life Sciences	Cat#17-5248-02
Gilder Copper grids, 400 Mesh	Ted Pella	Cat#G400
Half Area 96 Well Microplate	Corning	Cat#3679
HiLoad Superdex 75 PG 16/60	GE Healthcare Life Sciences	Cat#28989333
HiLoad Superdex 200 PG 16/60	GE Healthcare Life Sciences	Cat#28989335
Microplate Spectrophotometer	Tecan	Model: Safire
Superdex 200 Increase 5/150	GE Healthcare Life Sciences	Cat#28990945

TABLE WITH EXAMPLES FOR AUTHOR REFERENCE

REAGENT or RESOURCE	SOURCE	IDENTIFIER
Antibodies		
Rabbit monoclonal anti-Snail	Cell Signaling Technology	Cat#3879S; RRID: AB_2255011
Mouse monoclonal anti-Tubulin (clone DM1A)	Sigma-Aldrich	Cat#T9026; RRID: AB_477593
Rabbit polyclonal anti-BMAL1	This paper	N/A
Bacterial and Virus Strains		
pAAV-hSyn-DIO-hM3D(Gq)-mCherry	Krashes et al., 2011	Addgene AAV5; 44361-AAV5
AAV5-EF1a-DIO-hChR2(H134R)-EYFP	Hope Center Viral Vectors Core	N/A
Cowpox virus Brighton Red	BEI Resources	NR-88
Zika-SMGC-1, GENBANK: KX266255	Isolated from patient (Wang et al., 2016)	N/A
Staphylococcus aureus	ATCC	ATCC 29213

REAGENT or RESOURCE	SOURCE	IDENTIFIER
Streptococcus pyogenes: M1 serotype strain: strain SF370; M1 GAS	ATCC	ATCC 700294
Biological Samples		
Healthy adult BA9 brain tissue	University of Maryland Brain & Tissue Bank; http://medschool.umaryland.edu/btbank/	Cat#UMB1455
Human hippocampal brain blocks	New York Brain Bank	http://nybb.hs.columbia.edu/
Patient-derived xenografts (PDX)	Children's Oncology Group Cell Culture and Xenograft Repository	http://cogcell.org/
Chemicals, Peptides, and Recombinant Proteins		
MK-2206 AKT inhibitor	Selleck Chemicals	S1078; CAS: 1032350-13-2
SB-505124	Sigma-Aldrich	S4696; CAS: 694433-59-5 (free base)
Picrotoxin	Sigma-Aldrich	P1675; CAS: 124-87-8
Human TGF-β	R&D	240-B; GenPept: P01137
Activated S6K1	Millipore	Cat#14-486
GST-BMAL1	Novus	Cat#H00000406-P01
Critical Commercial Assays		
EasyTag EXPRESS 35S Protein Labeling Kit	Perkin-Elmer	NEG772014MC
CaspaseGlo 3/7	Promega	G8090
TruSeq ChIP Sample Prep Kit	Illumina	IP-202-1012
Deposited Data		
Raw and analyzed data	This paper	GEO: GSE63473
B-RAF RBD (apo) structure	This paper	PDB: 5J17
Human reference genome NCBI build 37, GRCh37	Genome Reference Consortium	http://www.ncbi.nlm.nih.gov/projects/genome/assembly/grc/human/
Nanog STILT inference	This paper; Mendeley Data	http://dx.doi.org/10.17632/wx6s4mj7s8.2
Affinity-based mass spectrometry performed with 57 genes	This paper; and Mendeley Data	Table S8; http://dx.doi.org/10.17632/5hvpvspw82.1
Experimental Models: Cell Lines		
Hamster: CHO cells	ATCC	CRL-11268
D. melanogaster: Cell line S2: S2-DRSC	Laboratory of Norbert Perrimon	FlyBase: FBtc0000181
Human: Passage 40 H9 ES cells	MSKCC stem cell core facility	N/A
Human: HUES 8 hESC line (NIH approval number NIHhESC-09-0021)	HSCI iPS Core	hES Cell Line: HUES-8
Experimental Models: Organisms/Strains		
C. elegans: Strain BC4011: srl-1(s2500) II; dpy-18(e364) III; unc-46(e177)rol-3(s1040) V.	Caenorhabditis Genetics Center	WB Strain: BC4011; WormBase: WBVar00241916
D. melanogaster: RNAi of Sxl: y[1] sc[*] v[1]; P{TRiP.HMS00609}attP2	Bloomington Drosophila Stock Center	BDSC:34393; FlyBase: FBtp0064874
S. cerevisiae: Strain background: W303	ATCC	ATTC: 208353
Mouse: R6/2: B6CBA-Tg(HDexon1)62Gpb/3J	The Jackson Laboratory	JAX: 006494
Mouse: OXTRfl/fl: B6.129(SJL)-Oxtr$^{tm1.1Wsy}$/J	The Jackson Laboratory	RRID: IMSR_JAX:008471
Zebrafish: Tg(Shha:GFP)t10: t10Tg	Neumann and Nuesslein-Volhard, 2000	ZFIN: ZDB-GENO-060207-1
Arabidopsis: 35S::PIF4-YFP, BZR1-CFP	Wang et al., 2012	N/A
Arabidopsis: JYB1021.2: pS24(AT5G58010)::cS24:GFP(-G):NOS #1	NASC	NASC ID: N70450
Oligonucleotides		
siRNA targeting sequence: PIP5K I alpha #1: ACACAGUACUCAGUUGAUA	This paper	N/A
Primers for XX, see Table SX	This paper	N/A
Primer: GFP/YFP/CFP Forward: GCACGACTTCTTCAAGTCCGCCATGCC	This paper	N/A
Morpholino: MO-pax2a GGTCTGCTTTGCAGTGAATATCCAT	Gene Tools	ZFIN: ZDB-MRPHLNO-061106-5
ACTB (hs01060665_g1)	Life Technologies	Cat#4331182
RNA sequence: hnRNPA1_ligand: UAGGGACUUAGGGUUCUCUCUAGGGACUUAGGGUUCUCUCUAGGGA	This paper	N/A

REAGENT or RESOURCE	SOURCE	IDENTIFIER
Recombinant DNA		
pLVX-Tight-Puro (TetOn)	Clonetech	Cat#632162
Plasmid: GFP-Nito	This paper	N/A
cDNA GH111110	Drosophila Genomics Resource Center	DGRC:5666; FlyBase:FBcl0130415
AAV2/1-hsyn-GCaMP6- WPRE	Chen et al., 2013	N/A
Mouse raptor: pLKO mouse shRNA 1 raptor	Thoreen et al., 2009	Addgene Plasmid #21339
Software and Algorithms		
Bowtie2	Langmead and Salzberg, 2012	http://bowtie-bio.sourceforge.net/bowtie2/index.shtml
Samtools	Li et al., 2009	http://samtools.sourceforge.net/
Weighted Maximal Information Component Analysis v0.9	Rau et al., 2013	https://github.com/ChristophRau/wMICA
ICS algorithm	This paper; Mendeley Data	http://dx.doi.org/10.17632/5hvpvspw82.1
Other		
Sequence data, analyses, and resources related to the ultra-deep sequencing of the AML31 tumor, relapse, and matched normal.	This paper	http://aml31.genome.wustl.edu
Resource website for the AML31 publication	This paper	https://github.com/chrisamiller/aml31SuppSite

Supplementary Material

Refer to Web version on PubMed Central for supplementary material.

Acknowledgments

We thank Sagar Kathuria for help with SAXS data collection and Gregory Hendricks, Lara Stritmatter, Chen Xu and Roger Craig at the UMASS EM core facility for technical support during EM data collection. This research was supported by NIH Grant GM056324 (to D.G.L) and used resources of the Advanced Photon Source, a U.S. Department of Energy (DOE) Office of Science User Facility operated for the DOE Office of Science by Argonne National Laboratory under Contract No. DE-AC02-06CH11357. “This project was supported by grant 9 P41 GM103622 from the National Institute of General Medical Sciences of the National Institutes of Health.” The content is solely the responsibility of the authors and does not necessarily reflect the official views of the National Institute of General Medical Sciences or the National Institutes of Health.

References

Aghazadeh B, Lowry WE, Huang XY, Rosen MK. Structural basis for relief of autoinhibition of the Dbl homology domain of proto-oncogene Vav by tyrosine phosphorylation. Cell. 2000; 102:625–633. [PubMed: 11007481]

Aizel K, Biou V, Navaza J, Duarte LV, Campanacci V, Cherfils J, Zeghouf M. Integrated conformational and lipid-sensing regulation of endosomal ArfGEF BRAG2. PLoS Biol. 2013; 11:e1001652. [PubMed: 24058294]

Alix E, Chesnel L, Bowzard BJ, Tucker AM, Delprato A, Cherfils J, Wood DO, Kahn RA, Roy CR. The capping domain in RalF regulates effector functions. PLoS Pathog. 2012; 8:e1003012. [PubMed: 23166491]

Amor JC, Swails J, Zhu X, Roy CR, Nagai H, Ingmundson A, Cheng X, Kahn RA. The structure of RalF, an ADP-ribosylation factor guanine nucleotide exchange factor from Legionella pneumophila, reveals the presence of a cap over the active site. J Biol Chem. 2005; 280:1392–1400. [PubMed: 15520000]

Berman HM, Westbrook J, Feng Z, Gilliland G, Bhat TN, Weissig H, Shindyalov IN, Bourne PE. The Protein Data Bank. Nucleic Acids Res. 2000; 28:235–242. [PubMed: 10592235]

Bernado P, Mylonas E, Petoukhov MV, Blackledge M, Svergun DI. Structural characterization of flexible proteins using small-angle X-ray scattering. J Am Chem Soc. 2007; 129:5656–5664. [PubMed: 17411046]

Betz SF, Schnuchel A, Wang H, Olejniczak ET, Meadows RP, Lipsky BP, Harris EA, Staunton DE, Fesik SW. Solution structure of the cytohesin-1 (B2-1) Sec7 domain and its interaction with the GTPase ADP ribosylation factor 1. Proc Natl Acad Sci U S A. 1998; 95:7909–7914. [PubMed: 9653114]

Booth DS, Avila-Sakar A, Cheng Y. Visualizing proteins and macromolecular complexes by negative stain EM: from grid preparation to image acquisition. J Vis Exp. 2011; (58):e3227.

Carter L, Kim SJ, Schneidman-Duhovny D, Stohr J, Poncet-Montange G, Weiss TM, Tsuruta H, Prusiner SB, Sali A. Prion Protein-Antibody Complexes Characterized by Chromatography-Coupled Small-Angle X-Ray Scattering. Biophys J. 2015; 109:793–805. [PubMed: 26287631]

Casanova JE. Regulation of Arf activation: the Sec7 family of guanine nucleotide exchange factors. Traffic. 2007; 8:1476–1485. [PubMed: 17850229]

Chardin P, Paris S, Antonny B, Robineau S, Beraud-Dufour S, Jackson CL, Chabre M. A human exchange factor for ARF contains Sec7- and pleckstrin-homology domains. Nature. 1996; 384:481–484. [PubMed: 8945478]

Cherfils J, Menetrey J, Mathieu M, Le Bras G, Robineau S, Beraud-Dufour S, Antonny B, Chardin P. Structure of the Sec7 domain of the Arf exchange factor ARNO. Nature. 1998; 392:101–105. [PubMed: 9510256]

Cherfils J, Zeghouf M. Regulation of small GTPases by GEFs, GAPs, and GDIs. Physiol Rev. 2013; 93:269–309. [PubMed: 23303910]

Cohen LA, Honda A, Varnai P, Brown FD, Balla T, Donaldson JG. Active Arf6 recruits ARNO/cytohesin GEFs to the PM by binding their PH domains. Mol Biol Cell. 2007; 18:2244–2253. [PubMed: 17409355]

Cronin TC, DiNitto JP, Czech MP, Lambright DG. Structural determinants of phosphoinositide selectivity in splice variants of Grp1 family PH domains. EMBO J. 2004; 23:3711–3720. [PubMed: 15359279]

Dierks H, Kolanus J, Kolanus W. Actin cytoskeletal association of cytohesin-1 is regulated by specific phosphorylation of its carboxyl-terminal polybasic domain. J Biol Chem. 2001; 276:37472–37481. [PubMed: 11438522]

DiNitto JP, Delprato A, Gabe Lee MT, Cronin TC, Huang S, Guilherme A, Czech MP, Lambright DG. Structural basis and mechanism of autoregulation in 3-phosphoinositide-dependent Grp1 family Arf GTPase exchange factors. Mol Cell. 2007; 28:569–583. [PubMed: 18042453]

DiNitto JP, Lambright DG. Membrane and juxtamembrane targeting by PH and PTB domains. Biochim Biophys Acta. 2006; 1761:850–867. [PubMed: 16807090]

Donaldson JG, Honda A. Localization and function of Arf family GTPases. Biochem Soc Trans. 2005; 33:639–642. [PubMed: 16042562]

Donaldson JG, Jackson CL. ARF family G proteins and their regulators: roles in membrane transport, development and disease. Nat Rev Mol Cell Biol. 2011; 12:362–375. [PubMed: 21587297]

Ferguson KM, Kavran JM, Sankaran VG, Fournier E, Isakoff SJ, Skolnik EY, Lemmon MA. Structural basis for discrimination of 3-phosphoinositides by pleckstrin homology domains. Mol Cell. 2000; 6:373–384. [PubMed: 10983984]

Franco M, Chardin P, Chabre M, Paris S. Myristoylation of ADP-ribosylation factor 1 facilitates nucleotide exchange at physiological Mg2+ levels. J Biol Chem. 1995; 270:1337–1341. [PubMed: 7836400]

Franke D, Svergun DI. DAMMIF, a program for rapid ab-initio shape determination in small-angle scattering. J Appl Crystallogr. 2009; 42:342–346. [PubMed: 27630371]

Fuss B, Becker T, Zinke I, Hoch M. The cytohesin Steppke is essential for insulin signalling in Drosophila. Nature. 2006; 444:945–948. [PubMed: 17167488]

Garzon JI, Kovacs J, Abagyan R, Chacon P. ADP_EM: fast exhaustive multi-resolution docking for high-throughput coverage. Bioinformatics. 2007; 23:427–433. [PubMed: 17150992]

Goldberg J. Structural basis for activation of ARF GTPase: mechanisms of guanine nucleotide exchange and GTP-myristoyl switching. Cell. 1998; 95:237–248. [PubMed: 9790530]

Gureasko J, Galush WJ, Boykevisch S, Sondermann H, Bar-Sagi D, Groves JT, Kuriyan J. Membrane-dependent signal integration by the Ras activator Son of sevenless. Nat Struct Mol Biol. 2008; 15:452–461. [PubMed: 18454158]

Gureasko J, Kuchment O, Makino DL, Sondermann H, Bar-Sagi D, Kuriyan J. Role of the histone domain in the autoinhibition and activation of the Ras activator Son of Sevenless. Proc Natl Acad Sci U S A. 2010; 107:3430–3435. [PubMed: 20133692]

Hafner M, Schmitz A, Grune I, Srivatsan SG, Paul B, Kolanus W, Quast T, Kremmer E, Bauer I, Famulok M. Inhibition of cytohesins by SecinH3 leads to hepatic insulin resistance. Nature. 2006; 444:941–944. [PubMed: 17167487]

Hashimoto S, Onodera Y, Hashimoto A, Tanaka M, Hamaguchi M, Yamada A, Sabe H. Requirement for Arf6 in breast cancer invasive activities. Proc Natl Acad Sci U S A. 2004; 101:6647–6652. [PubMed: 15087504]

Heller H, Schaefer M, Schulten K. Molecular dynamics simulation of a bilayer of 200 lipids in the gel and in the liquid crystal phase. The Journal of Physical Chemistry. 1993; 97:8343–8360.

Hiester KG, Santy LC. The cytohesin coiled-coil domain interacts with threonine 276 to control membrane association. PLoS One. 2013; 8:e82084. [PubMed: 24303080]

Kolanus W, Nagel W, Schiller B, Zeitlmann L, Godar S, Stockinger H, Seed B. Alpha L beta 2 integrin/LFA-1 binding to ICAM-1 induced by cytohesin-1, a cytoplasmic regulatory molecule. Cell. 1996; 86:233–242. [PubMed: 8706128]

Konarev PV, Volkov VV, Sokolova AV, Koch MHJ, Svergun DI. PRIMUS: a Windows PC-based system for small-angle scattering data analysis. J Appl Crystallogr. 2003; 36:1277–1282.

Kozin MB, Svergun DI. Automated matching of high- and low-resolution structural models. J Appl Crystallogr. 2001; 34:33–41.

Kremer JR, Mastronarde DN, McIntosh JR. Computer visualization of three-dimensional image data using IMOD. J Struct Biol. 1996; 116:71–76. [PubMed: 8742726]

Lawson CL, Patwardhan A, Baker ML, Hryc C, Garcia ES, Hudson BP, Lagerstedt I, Ludtke SJ, Pintilie G, Sala R, et al. EMDataBank unified data resource for 3DEM. Nucleic Acids Res. 2016; 44:D396–403. [PubMed: 26578576]

Lemmon MA. Pleckstrin homology domains: not just for phosphoinositides. Biochem Soc Trans. 2004; 32:707–711. [PubMed: 15493994]

Li J, Malaby AW, Famulok M, Sabe H, Lambright DG, Hsu VW. Grp1 plays a key role in linking insulin signaling to glut4 recycling. Dev Cell. 2012; 22:1286–1298. [PubMed: 22609160]

Lietzke SE, Bose S, Cronin T, Klarlund J, Chawla A, Czech MP, Lambright DG. Structural basis of 3-phosphoinositide recognition by pleckstrin homology domains. Mol Cell. 2000; 6:385–394. [PubMed: 10983985]

Liu Y, Kahn RA, Prestegard JH. Structure and membrane interaction of myristoylated ARF1. Structure. 2009; 17:79–87. [PubMed: 19141284]

Liu Y, Kahn RA, Prestegard JH. Dynamic structure of membrane-anchored Arf*GTP. Nat Struct Mol Biol. 2010; 17:876–881. [PubMed: 20601958]

Malaby AW, Chakravrthy S, Irving TC, Kathuria SV, Osman B, Lambright DG. Methods for analysis of size-exclusion chromatography-small angle X-ray scattering and reconstruction of protein scattering. J Appl Crystallogr. 2015; 48:1102–1113. [PubMed: 26306089]

Malaby AW, van den Berg B, Lambright DG. Structural basis for membrane recruitment and allosteric activation of cytohesin family Arf GTPase exchange factors. Proc Natl Acad Sci U S A. 2013; 110:14213–14218. [PubMed: 23940353]

Morin A, Eisenbraun B, Key J, Sanschagrin PC, Timony MA, Ottaviano M, Sliz P. Collaboration gets the most out of software. Elife. 2013; 2:e01456. [PubMed: 24040512]

Muralidharan-Chari V, Clancy J, Plou C, Romao M, Chavrier P, Raposo G, D'Souza-Schorey C. ARF6-regulated shedding of tumor cell-derived plasma membrane microvesicles. Curr Biol. 2009; 19:1875–1885. [PubMed: 19896381]

Nie Z, Hirsch DS, Randazzo PA. Arf and its many interactors. Curr Opin Cell Biol. 2003; 15:396–404. [PubMed: 12892779]

Ogasawara M, Kim SC, Adamik R, Togawa A, Ferrans VJ, Takeda K, Kirby M, Moss J, Vaughan M. Similarities in function and gene structure of cytohesin-4 and cytohesin-1, guanine nucleotide-exchange proteins for ADP-ribosylation factors. J Biol Chem. 2000; 275:3221–3230. [PubMed: 10652308]

Pasqualato S, Menetrey J, Franco M, Cherfils J. The structural GDP/GTP cycle of human Arf6. EMBO Rep. 2001; 2:234–238. [PubMed: 11266366]

Petoukhov MV, Franke D, Shkumatov AV, Tria G, Kikhney AG, Gajda M, Gorba C, Mertens HDT, Konarev PV, Svergun DI. New developments in the ATSAS program package for small-angle scattering data analysis. J Appl Crystallogr. 2012; 45:342–350. [PubMed: 25484842]

Petoukhov MV, Svergun DI. Global rigid body modeling of macromolecular complexes against small-angle scattering data. Biophys J. 2005; 89:1237–1250. [PubMed: 15923225]

Pettersen EF, Goddard TD, Huang CC, Couch GS, Greenblatt DM, Meng EC, Ferrin TE. UCSF Chimera--a visualization system for exploratory research and analysis. J Comput Chem. 2004; 25:1605–1612. [PubMed: 15264254]

Randazzo PA, Terui T, Sturch S, Fales HM, Ferrige AG, Kahn RA. The myristoylated amino terminus of ADP-ribosylation factor 1 is a phospholipid- and GTP-sensitive switch. J Biol Chem. 1995; 270:14809–14815. [PubMed: 7782347]

Raveh B, Enosh A, Schueler-Furman O, Halperin D. Rapid sampling of molecular motions with prior information constraints. PLoS Comput Biol. 2009; 5:e1000295. [PubMed: 19247429]

Renault L, Christova P, Guibert B, Pasqualato S, Cherfils J. Mechanism of domain closure of Sec7 domains and role in BFA sensitivity. Biochemistry. 2002; 41:3605–3612. [PubMed: 11888276]

Renault L, Guibert B, Cherfils J. Structural snapshots of the mechanism and inhibition of a guanine nucleotide exchange factor. Nature. 2003; 426:525–530. [PubMed: 14654833]

Richardson BC, Fromme JC. Autoregulation of Sec7 Arf-GEF activity and localization by positive feedback. Small GTPases. 2012; 3:240–243. [PubMed: 22996016]

Rosenthal PB, Henderson R. Optimal determination of particle orientation, absolute hand, and contrast loss in single-particle electron cryomicroscopy. J Mol Biol. 2003; 333:721–745. [PubMed: 14568533]

Russel D, Lasker K, Webb B, Velazquez-Muriel J, Tjioe E, Schneidman-Duhovny D, Peterson B, Sali A. Putting the pieces together: integrative modeling platform software for structure determination of macromolecular assemblies. PLoS Biol. 2012; 10:e1001244. [PubMed: 22272186]

Schneidman-Duhovny D, Hammel M, Tainer JA, Sali A. Accurate SAXS profile computation and its assessment by contrast variation experiments. Biophys J. 2013; 105:962–974. [PubMed: 23972848]

Sondermann H, Soisson SM, Boykevisch S, Yang SS, Bar-Sagi D, Kuriyan J. Structural analysis of autoinhibition in the Ras activator Son of sevenless. Cell. 2004; 119:393–405. [PubMed: 15507210]

Stalder D, Barelli H, Gautier R, Macia E, Jackson CL, Antonny B. Kinetic studies of the Arf activator Arno on model membranes in the presence of Arf effectors suggest control by a positive feedback loop. J Biol Chem. 2011; 286:3873–3883. [PubMed: 21118813]

Svergun D. Determination of the regularization parameter in indirect-transform methods using perceptual criteria. J Appl Crystallogr. 1992; 25:495–503.

Svergun D, Barberato C, Koch MHJ. CRYSOL - a Program to Evaluate X-ray Solution Scattering of Biological Macromolecules from Atomic Coordinates. J Appl Crystallogr. 1995; 28:768–773.

Svergun DI, Petoukhov MV, Koch MH. Determination of domain structure of proteins from X-ray solution scattering. Biophys J. 2001; 80:2946–2953. [PubMed: 11371467]

Tang G, Peng L, Baldwin PR, Mann DS, Jiang W, Rees I, Ludtke SJ. EMAN2: an extensible image processing suite for electron microscopy. J Struct Biol. 2007; 157:38–46. [PubMed: 16859925]

Tria G, Mertens HD, Kachala M, Svergun DI. Advanced ensemble modelling of flexible macromolecules using X-ray solution scattering. IUCrJ. 2015; 2:207–217.

Valentini E, Kikhney AG, Previtali G, Jeffries CM, Svergun DI. SASBDB, a repository for biological small-angle scattering data. Nucleic Acids Res. 2015; 43:D357–363. [PubMed: 25352555]

Volkov VV, Svergun DI. Uniqueness of ab initio shape determination in small-angle scattering. J Appl Crystallogr. 2003; 36:860–864.

Webb B, Sali A. Comparative Protein Structure Modeling Using MODELLER. Curr Protoc Bioinformatics. 2014; 47:5.6.1–32. [PubMed: 25199792]

Yu B, Martins IR, Li P, Amarasinghe GK, Umetani J, Fernandez-Zapico ME, Billadeau DD, Machius M, Tomchick DR, Rosen MK. Structural and energetic mechanisms of cooperative autoinhibition and activation of Vav1. Cell. 2010; 140:246–256. [PubMed: 20141838]

Highlights

- Structural dynamics of inactive and active Cytohesins investigated by SAXS and EM
- Hinge flexibility facilitates access to the activator binding site in the PH domain
- Conformational entropy in the Sec7-PH domain linker eposes the substrate site
- Structure-based model for allosteric activation and substrate engagement on membranes

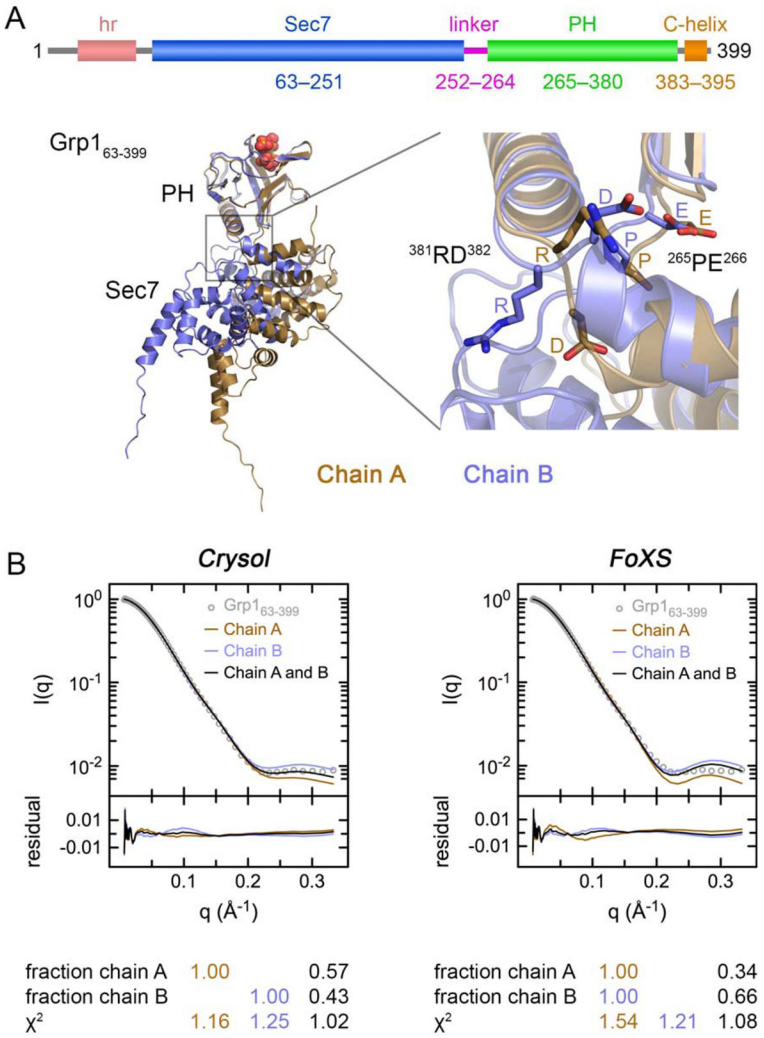

Figure 1. SAXS analysis of the autoinhibited Grp1 in solution versus crystal structure

(A) Conformational differences in the two molecules (chains A and B) in the asymmetric unit of the autoinhibited $Grp1_{63-399}$ crystal structure after superposition of the PH domains. The main conformational rearrangement involves rotation of the Sec7 domain by ~30° about a hinge consisting of residues ^{265}PE^{266} and ^{381}RD^{382} located at the junctions between the N- and C- termini of the PH domain and the autoinhibitory linker and C-terminal helix, respectively. (B) Fits of the experimental SAXS profile for $Grp1_{63-399}$ with the theoretical profiles for chains A and B alone or in combination using CRYSOL or FoXS. Combined fits were calculated in DELA as the least squares linear combination of the fitted CRYSOL or FoXS models for each chain alone. See also Figure S1A.

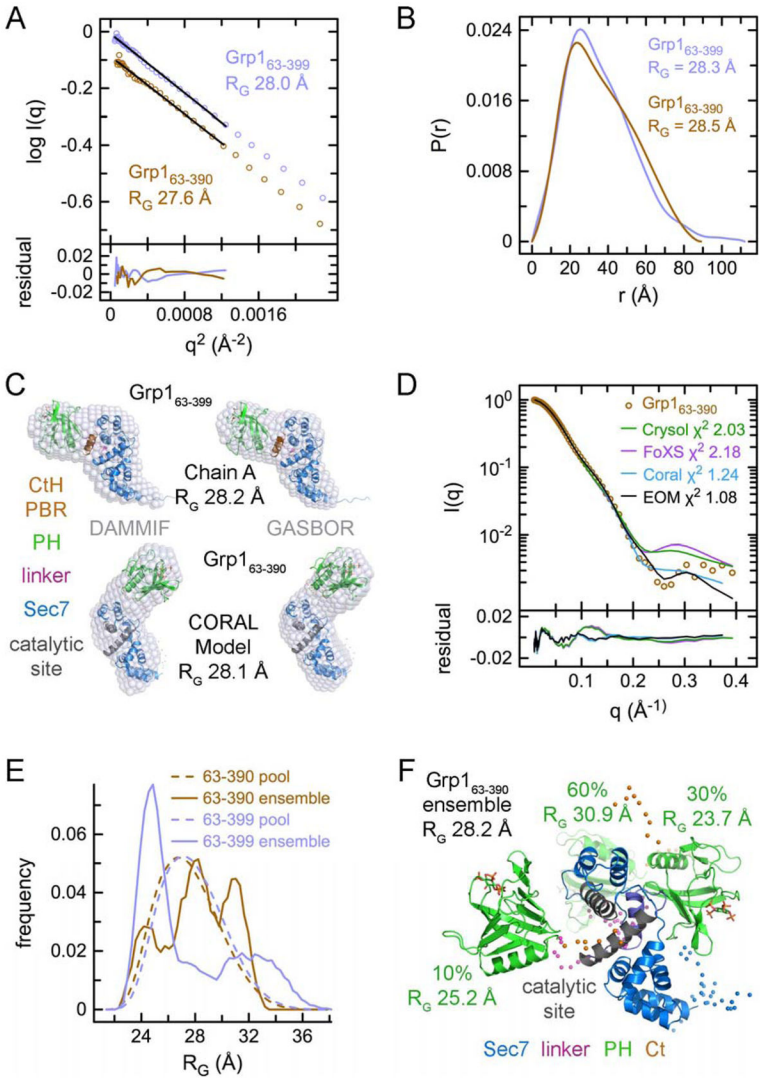

Figure 2. SAXS comparison of autoinhibited and active Grp1 constructs

(A) Guinier plots and fits for autoinhibited ($Grp1_{63-399}$) and active ($Grp1_{63-390}$) constructs. (B) P(r) distributions calculated with GNOM. (C) *Ab initio* bead models calculated with DAMMIF or GASBOR and aligned with the crystal structure ($Gpr1_{63-399}$) or rigid body model from CORAL ($Gpr1_{63-390}$). (D) Fits of the experimental scattering profile for $Grp1_{63-390}$ with profiles for theoretical models (CRYSOL and FoXS) derived by deleting the last nine residues from both chains in the $Grp1_{63-399}$ structure (PDB 2R09), the rigid body model (CORAL), and the best ensemble (EOM). (E) EOM R_G histograms for the pool and selected ensembles. (F) Best-fitting ensemble for $Grp1_{63-390}$ after superposition of the Sec7 domains (blue with catalytic site in gray). Note variation in the orientation of the PH domain (green). See also Figure S1.

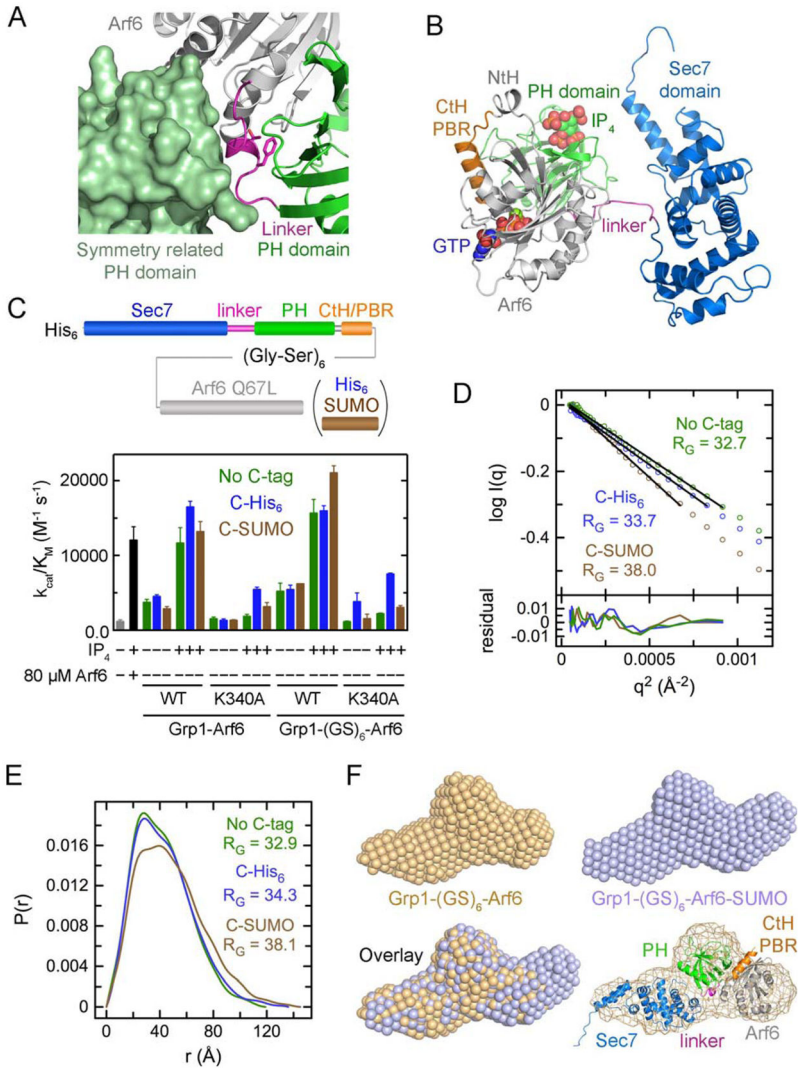

Figure 3. Design and validation of Grp1-Arf6 fusion constructs

(A) Intra/Inter-molecular interactions and crystal contacts involving the Sec7-PH linker in the $Grp1_{251-399}$ allosteric site complex with Arf6NΔ13-GppNHp (4KAX). (B) Model with good stereochemistry for a $Grp1_{63-399}$-Arf6 fusion construct generated with MODELLER. (C) Catalytic efficiency (k_{cat}/K_M) for $Grp1_{63-399}$-Arf6 fusion constructs with or without C-terminal tags compared with the isolated $Grp1_{63-399}$ in the presence or absence of 80 μM Arf6NΔ13-GppNHp and/or 10 μM IP_4. Bars and error bars represent the mean and standard deviation for three experiments. (D and E) Guinier plots/fits (D) and P(r) distributions (E) for the $Grp1_{63-399}$-6GS-Arf6 fusion constructs with the six Gly-Ser linker. (F) Comparison of *ab initio* bead models calculated with DAMMIF for the $Grp1_{63-399}$-6GS-Arf6 fusion with and without the C-terminal SUMO tag. Shown on the lower right is the result of manually docking the Sec7 domain and allosteric site-Arf6 complex into the envelope for the $Grp1_{63-399}$-6GS-Arf6 *ab initio* bead model. See also Figures S2 and S3.

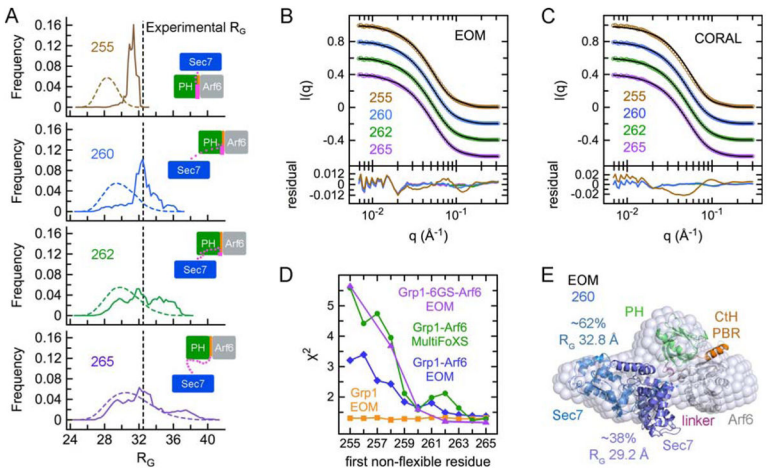

Figure 4. Rigid body and ensemble modeling of Sec7-PH linker flexibility in Grp1-Arf6 fusions

(A) EOM R_G histograms for the pool (dashed lines) and selected ensembles (solid lines) of Grp1-6GS-Arf6 fusions with an increasing number of linker residues treated as flexible. The first non-flexible linker residue is indicated for each histogram pair. The experimental R_G determined by Guinier analysis is shown as a black dashed-line. (B and C) Comparison of the experimental SAXS profile for the Grp1-6GS-Arf6 construct with the scattering profile (black lines) for the best-fitting EOM ensemble (B) or rigid body CORAL model (C) with the indicated first non-flexible linker residue. (D) Systematic analysis of χ^2 for best-fitting ensembles as a function of increasing linker flexibility. (E) Best fitting ensemble for the Grp1-Arf6 fusion with 260 as the first non-flexible linker residue after superposition of the PH-Arf6 domains and alignment of the *ab initio* bead model with the most frequent model. See also Figures S2 and S3.

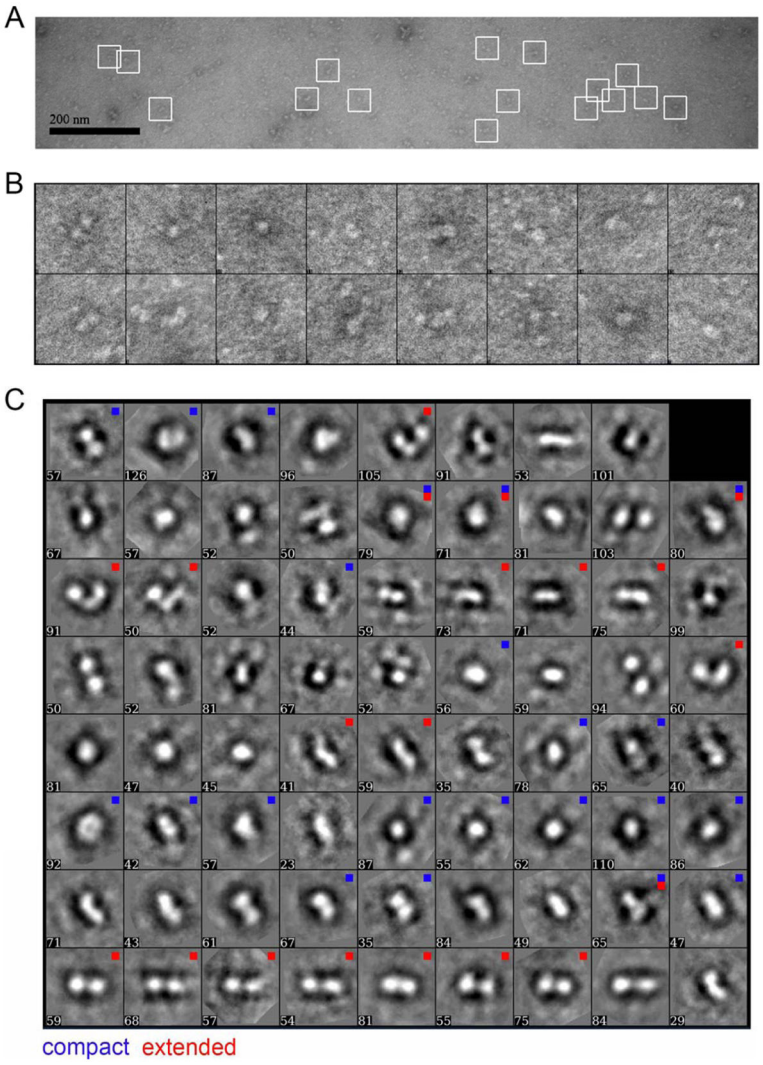

Figure 5. NS-EM micrograph and class averages for the active Grp1-Arf6 fusion

(A) Representative area of micrograph illustrating active $Grp1_{63-399}$-Arf6 fusion particles stained with uranyl formate. Boxes indicate representative examples of selected particles. (B) Enlarged views of boxed particles in A. (C) Unsupervised 2D class averages of manually-picked particles. Blue and red squares denote sets of classes used for 3D reconstruction of compact (blue) and extended (red) conformations. Particle numbers for each class are also indicated. See also Figure S4.

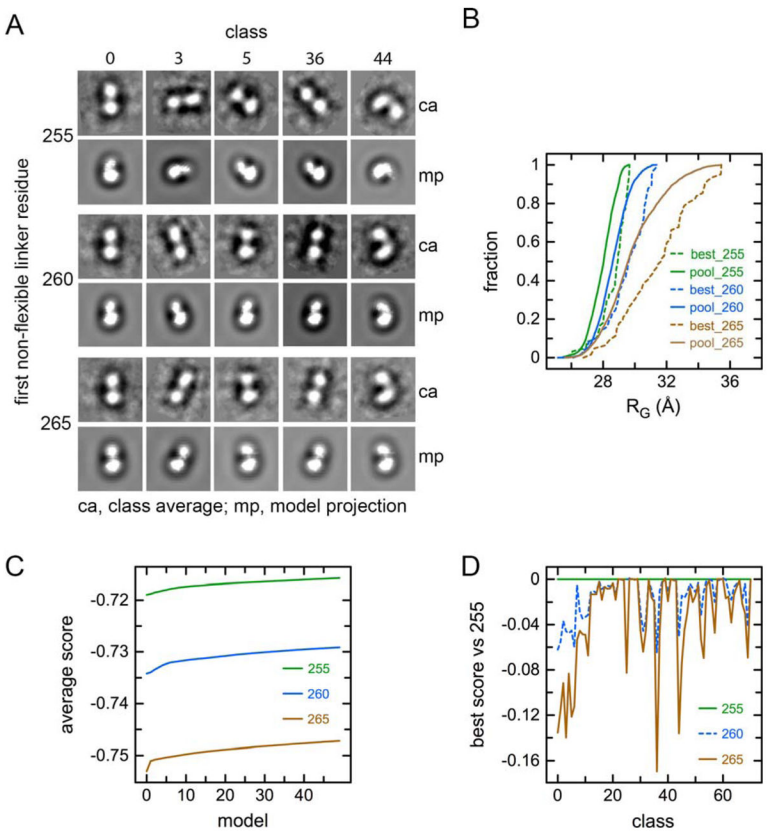

Figure 6. Projection matching analysis of MultiFoXS models with NS-EM particle classes for the active Grp1-Arf6 fusion

(A) Examples of class averages compared with the best scoring 3D volume projection of the models in the MultiFoXS pools with 255, 260 or 265 as the first non-flexible residue. (B) Cumulative distribution of R_G values corresponding to the best scoring models from the MultiFoXS pools for each of the 71 class averages. (C) Overall mean of scores for the best scoring models. (D) Best scores for each class after subtracting the corresponding best score for the MultiFoXS pool with 255 as the first non-flexible residue. See also Figures S4 and Figure S5.

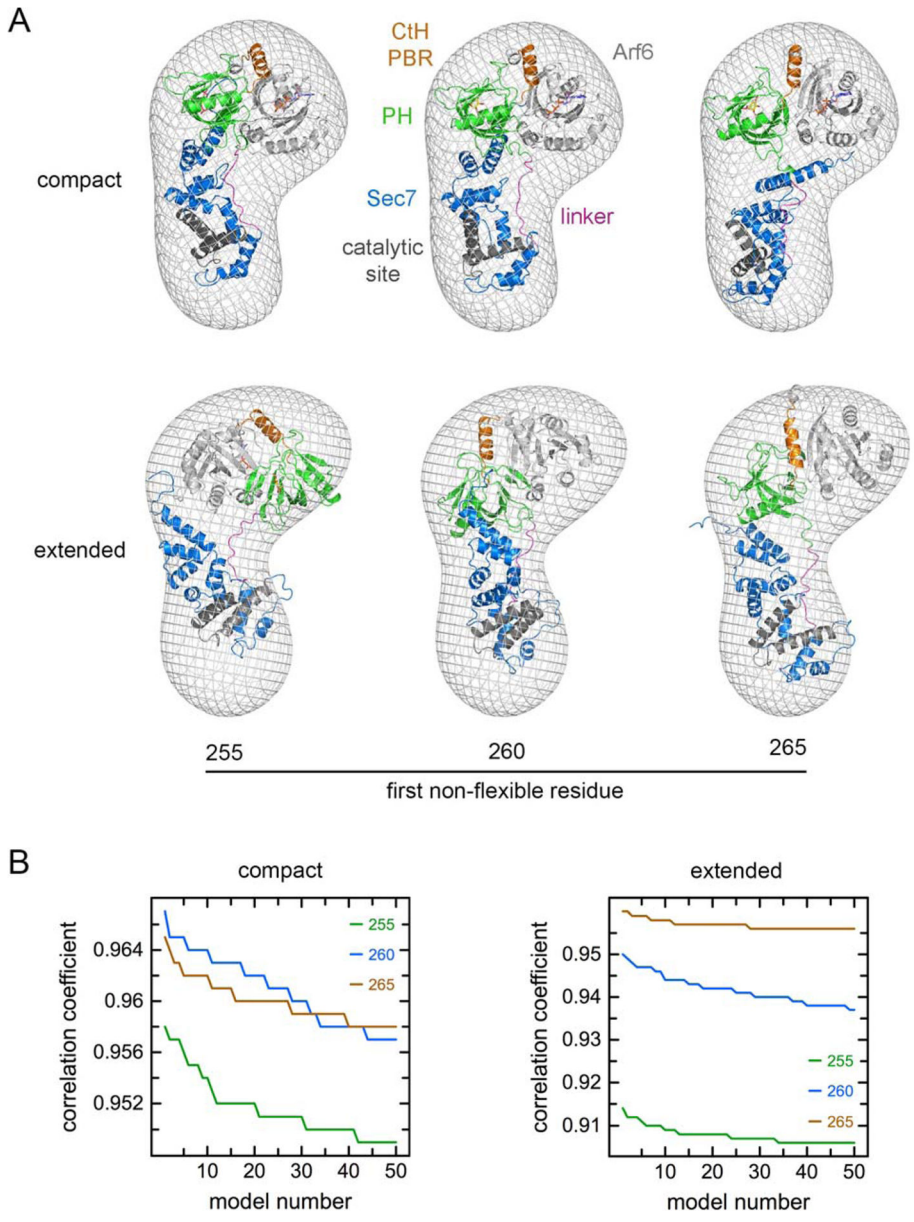

Figure 7. 3D reconstruction and comparison with MultiFoXS models

(A) Refined volumes for 3D reconstructions with the compact and extended sets of classes. Also shown are the best-fitting MultiFoXS models from the pools with 255, 260 and 265 as the first non-flexible linker residue. (B) Correlation coefficients for comparison of the refined volumes with the top 50 best-fitting MultiFoXS models. See also Figures S4, S6 and S7.

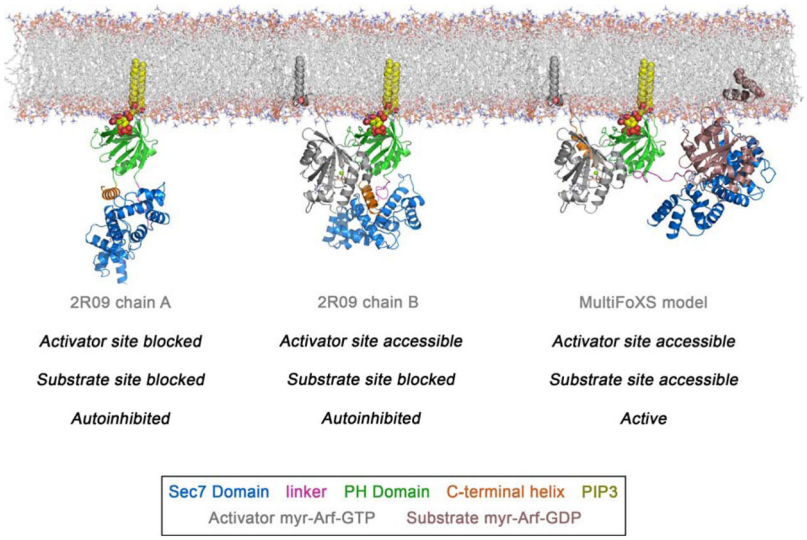

Figure 8. Model for membrane recruitment and allosteric activation

Left, model based on chain A from the crystal structure of autoinhibited $Grp1_{63-399}$ (2R09). The Arf6-GTP binding site in the PH domain is blocked due to a steric conflict between the C-terminal helix of Grp1 and the switch II helix of Arf6. ***Middle***, composite model for a putative intermediate complex between autoinhibited Grp1 and Arf-GTP based on chain B from the crystal structure of autoinhibited $Grp1_{63-399}$ (2R09) and Arf6-GTP acquired from the crystal structure of the Grp1 allosteric site complex with Arf6-GTP (2KAX) after superposition of the PH domains. In this autoinhibited Grp1 conformation, the Arf6-GTP binding site in the PH domain is accessible. ***Right***, composite model for Arf-GTP activated Grp1 in complex with an Arf-GDP substrate based on the most frequent MultiFoXS model from the pool with 260 as the first non-flexible linker residue and Arf1-GDP acquired from the crystal structure of the ARNO Sec7 domain (catalytic glutamate to lysine mutation) in complex with Arf1-GDP (1R8S) after superposition of the Sec7 domains. The acyl chains of PIP3 and myristolylated N-terminal helices of Arf GTPases were modeled in arbitrary configurations consistent with membrane partitioning and reasonable stereochemistry. The POPC bilayer membrane was derived from the coordinates of a molecular dynamics simulation (Heller et al., 1993).